

Constructing built-in electric field to accelerate the asymmetric local charge distribution for efficient alkaline overall water/seawater splitting

Zhuoping Wang, Shuai Wang*

School of Chemistry and Chemical Engineering, Huazhong University of Science and Technology, Wuhan 430074, PR China



ARTICLE INFO

Keywords:

Built-in electric field
Work function regulation
Interface engineering
Overall water/seawater splitting
Electrocatalyst

ABSTRACT

Developing efficient and durable bifunctional electrocatalysts for large-scale alkaline water/seawater electrolysis is essential but remains a challenge. Here, we have ingeniously constructed Mott-Schottky heterogeneously nanowire arrays consisting of Ru and Fe co-doped CoP with Ru nanoparticles (Ru/Ru_xFe-CoP). The incorporation of guest Ru and Fe atoms effectively increases the work function difference between the CoP region and the Ru region, leading to the enhancement of the built-in electric field, which accelerates the induction of electron transfer at the Mott-Schottky interface and promotes the formation of local electrophilic/nucleophilic region. Theoretical calculations revealed that the asymmetric charge distribution effectively modulated the free energy of hydrogen adsorption as well as the formation energy of oxygen intermediates. Benefiting from the regulation of local charge distribution, the constructed Ru/Ru_xFe-CoP exhibits a remarkable catalytic activity for HER and OER in 1 M KOH with overpotentials of only 146 and 345 mV at 1000 mA cm⁻², respectively. This innovative manipulation of charge asymmetric distribution by modulating Schottky heterojunctions provides an avenue for rational design of efficient bifunctional electrocatalysts.

1. Introduction

Hydrogen (H₂) is widely recognized as the most optimal energy carrier for future energy conversion systems due to its high energy density and zero carbon emission, primarily owing to its exceptional energy density and complete absence of carbon emissions [1–3]. Although the electrolysis of water for hydrogen generation is considered an ecologically sustainable technique, its widespread implementation in industrial settings may exacerbate the scarcity of freshwater resources due to the need for a substantial quantity of high-purity freshwater [4, 5]. Seawater, which accounts for 96.5% of world water resources, provides the vision of large-scale seawater hydrogen generation [6–9]. However, the complex composition of seawater severely restricts the efficiency of water splitting, since the presence of chloride ions causes chloride evolution reaction (CER) at high potentials to compete with oxygen evolution reaction (OER) [10,11]. In alkaline media, there is a maximum thermodynamic potential difference of 480 mV between CER and OER [12]. To meet the requirements for large-scale seawater hydrogen production, OER catalysts need to achieve high current density output at an overpotential lower than 480 mV [13,14]. On the other hand, the process of HER also faces the challenge of overcoming the

barrier of water dissociation in alkaline media [15–17]. Therefore, improved catalytic performance and stability of electrocatalysts, particularly bifunctional electrocatalysts, are essential for seawater electrolysis.

In recent decades, much attention has been dedicated to the investigation of effective bifunctional electrocatalysts. Transition metal phosphides (TMPs) have garnered significant interest owing to their low cost, exceptional chemical stability, and tunable structural composition [18,19]. Moreover, TMPs have been proven to repel chloride ions, which makes them a good electrocatalyst candidate for seawater splitting [20]. However, the intrinsic catalytic activity of TMPs is unsatisfactory, and the manipulation of the electronic structure through the introduction of heteroatoms is a widely employed approach to enhance the inherent reactivity [21–25]. Extensive research has demonstrated that the incorporation of Fe into TMPs can greatly augment their catalytic activity for OER [26–28]. Nevertheless, a single non-precious metal doping alone seems to be insufficient to change the overall water splitting performance of TMP-based catalysts. Ruthenium (Ru) has received more attention due to its cost advantage and the unique d-electronic structure of Ru resulting in a low water dissociation barrier, which contributes to making it the most promising alkaline HER electrocatalyst [29–31].

* Corresponding author.

E-mail address: chmsamuel@hust.edu.cn (S. Wang).

However, the excessive binding strength between Ru and H makes hydrogen desorption on the Ru surface challenging [32,33]. Enhancing the electron transport from the carrier to Ru can effectively weaken the hydrogen adsorption strength on the Ru site [34,35]. Therefore, a rational design of TMP to adjust the local charge density of Ru is the key to improving its HER performance.

Heterostructure engineering is considered an effective strategy to improve bifunctional electrocatalytic activity [19,36–38]. The electronic structure of the active site can be effectively modulated to balance the adsorption strength of the reaction intermediates by combining two hetero components with different Fermi levels to construct a built-in electric field [39–41]. Specifically, due to the mismatch in the work function, a Mott Schottky barrier will be generated at the heterointerface formed by the TMPs and the metal. Electrons spontaneously cross the interface, driven by the energy difference, and accumulate on the other side until the work function on both sides achieves equilibrium [42–44]. This process eventually leads to the establishment of a built-in electric field and a stable localized electrophilic/nucleophilic region near the interface [45,46]. The catalysts with negatively charged surfaces may be more inclined to interact with hydrogen for superior HER performance, whereas a positive charge on the catalyst surface favours the adsorption of OER intermediates [47]. Recently, Zhang et al. optimized the adsorption of hydrogen/oxygen intermediates by integrating Ni₂P and CoCH components with large differences in the work functions to form a stable built-in electric field at the interface [48]. Chen et al. constructed a CoO/Mo₂C epitaxial heterojunction catalyst, which induced the redistribution of interfacial electrons through the work functions and achieved excellent HER/OER catalytic performance [49]. Therefore, as a proof-of-concept, the rational construction of Mott-Schottky heterojunctions between Ru and TMP can enhance charge transport and separation, and the redistributed charges will significantly improve the adsorption behaviour of the reaction intermediates, leading to enhanced catalytic activity and selectivity.

Herein, we employ defect engineering and precisely control the phosphorization process to ingeniously construct a Mott-Schottky heterogeneous nanowire array catalyst consisting of Ru-Fe dual doped CoP with Ru nanoparticles (denoted as Ru/Ru,Fe-CoP). The incorporation of guest Ru and Fe atoms not only improves the intrinsic catalytic activity of the host CoP but also facilitates charge transfer from Ru,Fe-CoP region to Ru region, and this asymmetric interfacial charge distribution effectively improves the HER and OER activities. The as-prepared Ru/Ru,Fe-CoP exhibits excellent HER and OER activities in 1 M KOH with overpotentials of only 146 and 345 mV at 1000 mA cm⁻², respectively, as well as satisfactory bifunctional activity and long-term durability in alkaline seawater media. Density-functional theory (DFT) calculations demonstrate that the Mott-Schottky interface with asymmetric charge distribution optimizes the hydrogen adsorption free energy and lowers the formation energy barrier of OOH intermediates, which increases the HER and OER, respectively. In addition, the electrolyzer constructed with Ru/Ru,Fe-CoP as cathode and anode only requires 1.65 V to generate a current density of 500 mA cm⁻² in 1 M KOH freshwater and 1 M KOH seawater electrolytes, respectively. Furthermore, it has shown impressive stability and achieves high Faraday efficiency of approximately 97.1%. This work paves the way for the rational design of efficient bifunctional water splitting electrocatalysts by precisely constructing Mott-Schottky heterogeneous interfaces to enhance the built-in electric field.

2. Experimental section

2.1. Synthesis of CoFeAl-LDH nanowire arrays

CoFeAl-LDH nanowire arrays are synthesized by a typical hydrothermal method. The synthesis scheme is as follows: 3 mmol of Co (NO₃)₂·6 H₂O, 1 mmol of Fe(NO₃)₃·9 H₂O, and a certain amount of Al (NO₃)₃·9 H₂O are dissolved in 40 mL of deionized water, followed by the

addition of 0.371 g of NH₄F and 1.2 g of urea, and ultrasonication is carried out for 5 min, and then transferred to a 50 mL polytetrafluoroethylene inner liner after the formation of a clarified solution. Afterwards, 2×3 cm² of cleaned nickel foam is suspended in the inner liner and sealed into a stainless steel hydrothermal kettle, and the reaction is carried out at 120 °C for 6 h. After the reaction is completed and cooled down to room temperature, the excess product on the surface is washed with deionized water and dried in an oven at 60 °C to obtain the CoFeAl-LDH-x nanowire arrays grown on the nickel foam. x is denoted as the Al (NO₃)₃ addition, which is 0.20 mmol, 0.25 mmol, and 0.30 mmol, respectively.

2.2. Synthesis of CoFe^{vac}-LDH nanowire arrays

The obtained CoFeAl-LDH-x nanowire arrays are immersed in 2 M NaOH solution and reacted for 30 min to completely remove the Al element, and after the reaction is completed, they are removed from the NaOH solution, rinsed with a large amount of deionized water to wash away the remaining NaOH as well as the impurity ions on the surface, and dried at 60 °C, to obtain the CoFe^{vac}-LDH-x nanowire arrays, and x denotes that the products are obtained from the precursors obtained with different Al(NO₃)₃ additions, with x being 0.20, 0.25, and 0.30, respectively.

2.3. Synthesis of Ru/CoFe^{vac}-LDH nanowire arrays

The CoFe^{vac}-LDH-x nanowire arrays are immersed into a 1 mg·mL⁻¹ RuCl₃ solution and reacted for 5 min, and after washing off the excess RuCl₃ on the surface with deionized water, they are dried to obtain the Ru/CoFe^{vac}-LDH-x nanowire arrays, with the x of 0.20 and 0.25, respectively.

2.4. Synthesis of Ru/Ru,Fe-CoP and Ru,Fe-CoP nanowire arrays

The Ru/CoFe^{vac}-LDH-0.25 nanowire array is placed downstream of the tube furnace, and 2 g of NaHPO₂ is placed upstream, and the temperature is increased to 400 °C at a rate of 2 °C·min⁻¹ and held for 2 h to obtain Ru/Ru,Fe-CoP. Ru/CoFe^{vac}-LDH-0.20 nanowire array is phosphatized in the same way to obtain Ru,Fe-CoP. The Ru contents of Ru/Ru,Fe-CoP and Ru,Fe-CoP are about 10.2 wt% and 8.6 wt%, respectively, according to ICP-OES.

2.5. Materials characterization

Field emission transmission electron microscopy (TEM) and high-resolution TEM (HRTEM) studies were performed using a JEOL JEM 2100 F transmission electron microscope operated at 200 kV. X-ray diffraction (XRD) was recorded on a SmartLab-SE Xray diffractometer with Cu K α radiation ($\lambda=0.15419$ nm). X-ray photoelectron spectroscopy (XPS) signal was tested with Thermo ESCALAB 250XI. Element content was detected by using an inductively coupled plasma-optical emission spectroscopy (ICP-OES) on Thermo Scientific iCAP7200plus.

2.6. Electrochemical measurement

All HER and OER tests are obtained in standard three-electrode test system from a CHI 760E electrochemical workstation. The Ru/Ru,Fe-CoP is used as the work electrode. The graphite rod electrode and the Hg/HgO electrode are served as counter electrode and reference electrode, respectively. The linear sweep voltammetry (LSV) polarization curves are recorded with 80% iR compensation in three types of electrolytes (1 M KOH, 1 M KOH + 0.5 M NaCl, and 1 M KOH seawater) at a scan rate of 2 mV s⁻¹. The natural seawater was collected from Qingdao, Shandong, China. All measured potentials are converted to a reversible hydrogen electrode (RHE) according to the following equations:

$$E_{vs\text{--}RHE} = E_{vs\text{--}Hg/HgO} + E_{Hg/HgO}^0 + 0.0591 \times pH$$

The chronopotentiometry tests are measured at a constant current density of 100 and 500 mA cm⁻². Electrochemical active surface area (ECSA) was evaluated based on double-layer capacitance (C_{dl}) by CV in a non-Faradaic region with scan rates ranging from 20 to 100 mV s⁻¹. The ECSA of catalysts are calculated from the following equation:

$$ESCA = \frac{C_{dl(catalyst)} \text{ mF cm}^{-2}}{40\mu F \text{ cm}^{-2} \text{ per } ESCA \text{ cm}^{-2}}$$

The TOF is calculated by using the formula:

$$TOF(H_2 \text{ / s}) = \frac{\# \text{total hydrogen turnover per geometric area}}{\# \text{active sites per geometric area}}$$

2.7. Density functional theory (DFT) calculations

We have employed the VASP[50,51] to perform all the density functional theory (DFT) calculations within the generalized gradient approximation (GGA) using the Perdew-Burke-Ernzerhof (PBE)[52] formulation. We have chosen the projected augmented wave (PAW) potentials[53] to describe the ionic cores. Take valence electrons into account using a plane wave basis set with a kinetic energy cutoff of 450 eV. Partial occupancies of the Kohn–Sham orbitals were allowed using the Gaussian smearing method and a width of 0.05 eV. The electronic energy was considered self-consistent when the energy change was smaller than 10⁻⁵ eV. A geometry optimization was considered convergent when the energy change was smaller than 0.05 eV/Å. The Brillouin zone is sampled with 2 × 2 × 1 Monkhorst mesh [54].

Gibbs free energy can be obtained by adding corrections including entropic (TS) and zero-point energy (ZPE) to calculated DFT energy, so that $\Delta G = \Delta E_{DFT} + \Delta ZPE - T\Delta S - eU$, where the E_{DFT} is the calculated DFT reaction energy, ΔZPE is the change in ZPE calculated from the vibrational frequencies and ΔS is the change in the entropy referring to thermodynamics databases. The electrode potential are adopted with respect to the reversible hydrogen electrode, which makes the standard electrochemical potential of electron involved in reaction (Ge) equal to $-eU$, and the standard electrochemical potential of the proton (G_{H+}) equal to that of the hydrogen atom in gaseous H₂ (1/2 G_{H2}). Considering that the triplet state of the O₂ molecule is poorly described in the current DFT scheme, the free energy of the O₂ molecule was derived according to $G_{O2} = 2 G_{H2O} - 2 G_{H2} + 4.92$.

3. Result and discussion

3.1. Synthesis and structure characterization

The synthesis process of Ru/Ru,Fe-CoP Mott-Schottky heterojunction nanowire array catalysts is illustrated schematically in Fig. 1. Ni foam is an optimal carrier for catalysts on account of its substantial specific surface area, low cost, and exceptional electrical conductivity. Firstly, CoFeAl-LDH-x nanowire arrays (where x represents a different amount of Al) were uniformly grown on the surface of nickel foams by the hydrothermal method, and then CoFe^{vac}-LDH-x with abundant vacancy defects was obtained after the Al was removed by NaOH etching. In this procedure, the variations in Al contents will lead to different results after NaOH etching (see Supporting Information for more details). In particular, CoFe^{vac}-LDH-0.20 and CoFe^{vac}-LDH-0.25 preserves its structural stability while possessing a significant presence of vacancy defects (Figure S4). When immersed in the RuCl₃ solution, Ru³⁺ ions are trapped in the vacancy defects effectively, thus obtaining Ru/CoFe^{vac}-LDH-0.20 and Ru/CoFe^{vac}-LDH-0.25. The XRD patterns show that the characteristic diffraction peaks of Ru/CoFe^{vac}-LDH-0.20 and Ru/CoFe^{vac}-LDH-0.25 exhibit obvious shifts in small-angle directions, which proves that the successful incorporation of Ru leads to the expansion of the LDH lattice (Figure S5). In contrast, the XRD diffraction peaks of CoFe-LDH without vacancies are not significantly shifted after immersion in RuCl₃ solution. Therefore, the presence of vacancy defects is a necessary requirement for the successful incorporation of Ru atoms into LDH lattice. Finally, Ru/CoFe^{vac}-LDH-0.25 is converted into Ru/Ru,Fe-CoP Mott-Schottky heterojunction nanowire array catalysts at a phosphatization temperature of 400 °C, while Ru,Fe-CoP and Fe-CoP are comparison samples prepared by phosphating Ru/CoFe^{vac}-LDH-0.20 and Fe-CoP, respectively, under identical conditions (Figure S6).

The scanning electron microscope (SEM) images of Ru/CoFe^{vac}-LDH-0.25 and Ru/Ru,Fe-CoP are displayed in Fig. 2a-b. The Ru/CoFe^{vac}-LDH nanowires grow uniformly on the open porous skeletal structure of the nickel foams, whereas the bare Ni foams possess only an almost smooth surface (Figure S1). The morphology of the obtained Ru/Ru,Fe-CoP is well maintained after phosphatization (Fig. 2b). The 3D nanowire array has a significantly porous structure that promotes the efficient diffusion and penetration of the electrolyte. Despite the formation of insoluble precipitates during the process of seawater electrolysis, it guarantees the availability of numerous active sites and provides a flexible and fast channel for electron transport. Furthermore, the three-dimensional array structure also serves to efficiently facilitate the desorption of gases, thus enhancing the overall water splitting activity at high current density. Transmission electron microscopy (TEM) is employed for further investigation of the morphology and structural composition of

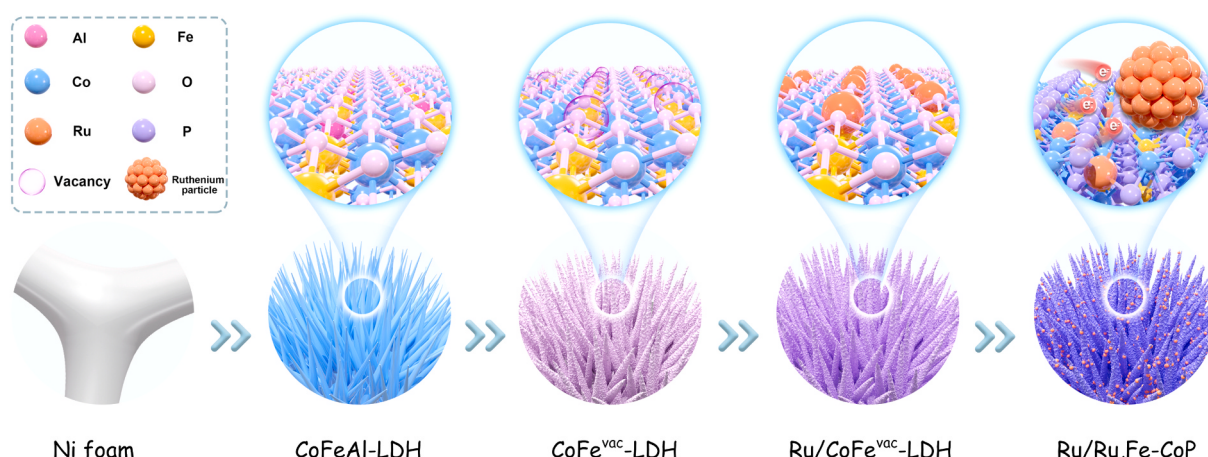


Fig. 1. Schematic illustration of the synthesis of Ru/Ru,Fe-CoP electrodes.

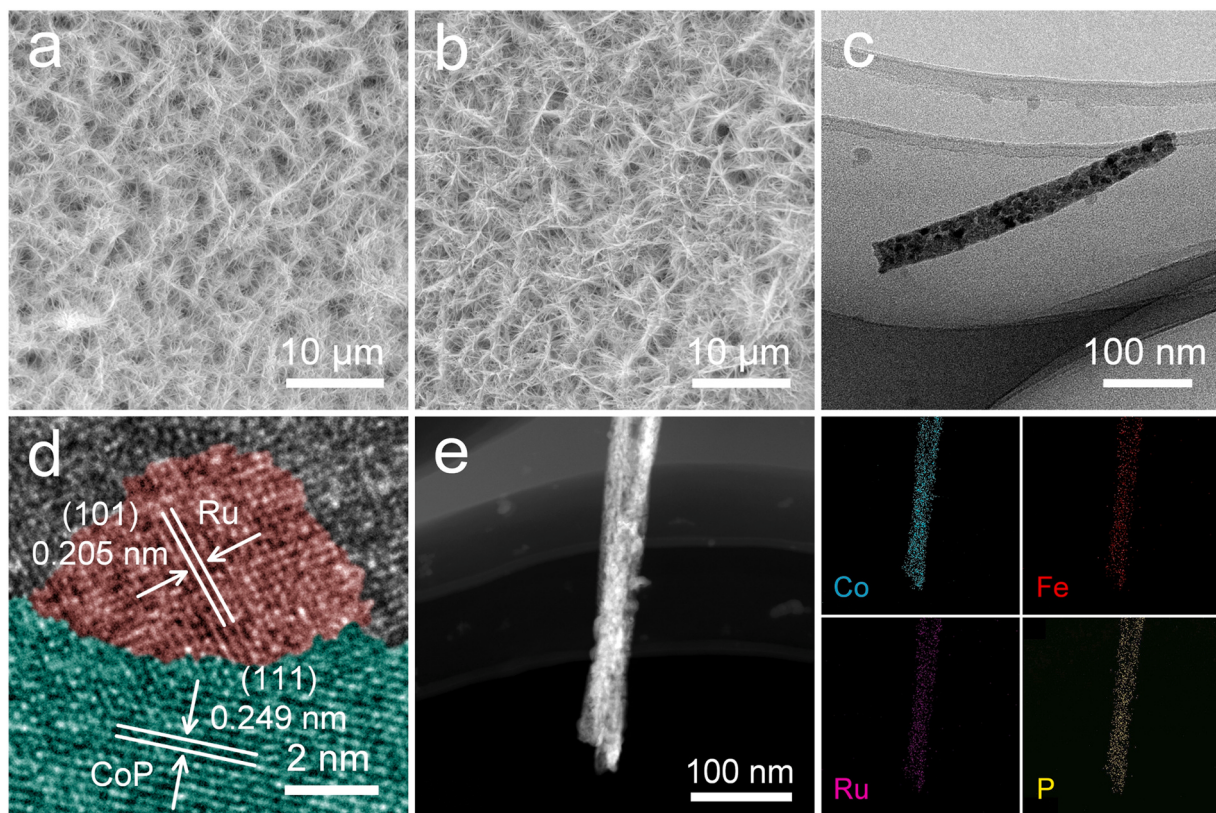


Fig. 2. a) SEM images of Ru/CoFe^{vac}-LDH, b) SEM images of Ru/Ru,Fe-CoP, c) TEM image of Ru/Ru,Fe-CoP, d) HRTEM image of Ru/Ru,Fe-CoP, e) EDS elemental mapping images of Ru/Ru,Fe-CoP.

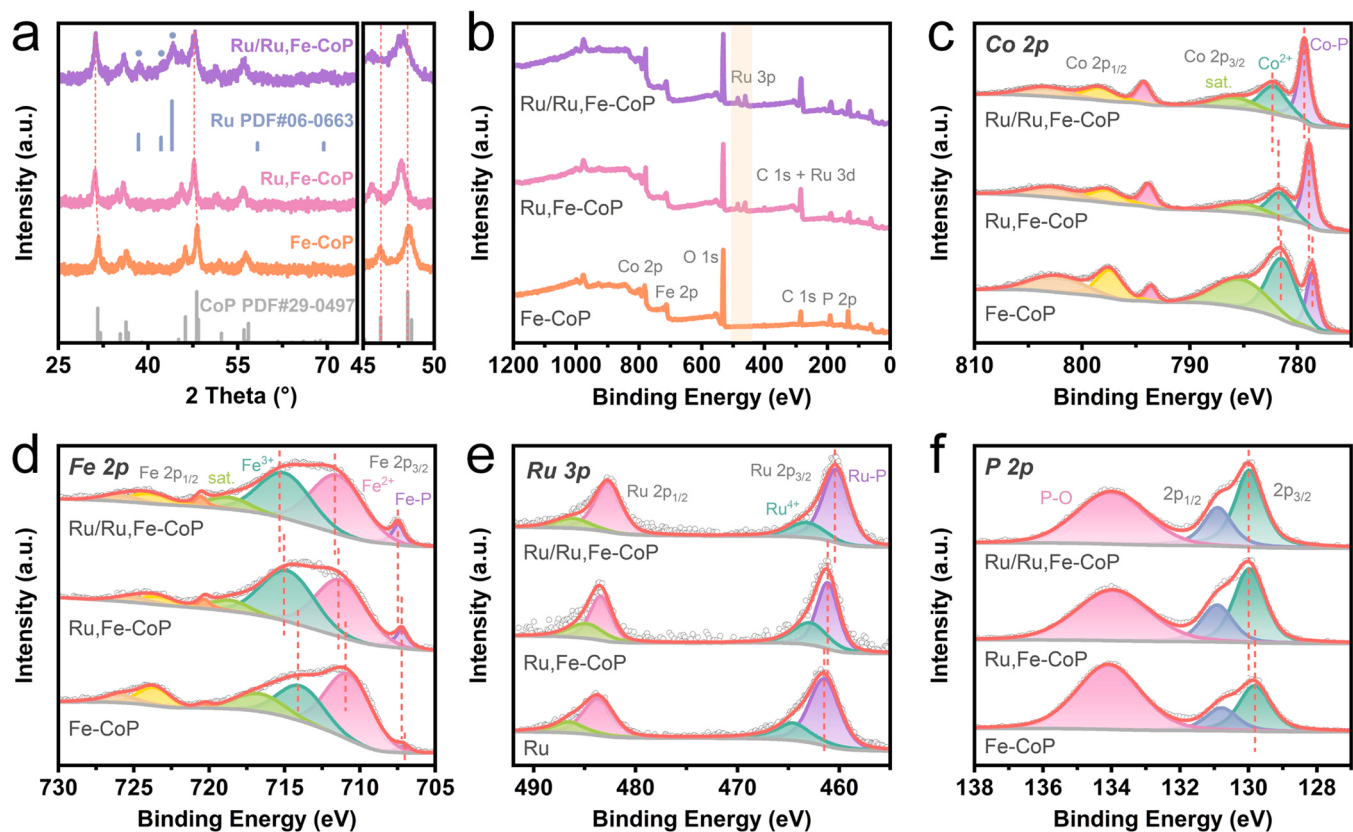


Fig. 3. Structural characterizations of Ru/Ru,Fe-CoP, Ru,Fe-CoP and Fe-CoP. a) XRD pattern. b) XPS surveys. c-f) high-resolution XPS spectra of c) Co 2p, d) Fe 2p, e) Ru 3p, and f) P 2p.

the catalysts. As shown in Fig. 2c, the dimensions of the Ru/Ru_xFe-CoP nanowire are approximately 50 nm in diameter and 300 nm in length, consistent with the morphology observed in SEM. The high-resolution transmission electron microscopy (HRTEM) image reveals a well-defined heterogeneous interface in Ru/Ru_xFe-CoP (Fig. 2d). Specifically, the lattice stripe with a spacing of 0.205 nm corresponds to the (101) crystal plane of the Ru nanoparticles, and the lattice stripe with a spacing of 0.249 nm can be attributed to the (111) crystal plane of the CoP. Notably, the lattice stripe of the CoP is slightly larger than that of the pristine CoP, potentially resulting from the doping of Ru and Fe, which induces an expansion in the CoP lattice spacing. The dark-field transmission electron microscopy images and the corresponding EDS elemental mapping further proved that Co, Fe, Ru, and P are uniformly distributed in the catalyst (Fig. 2e).

XRD analysis is essential to further confirm the phase structure of Ru/Ru_xFe-CoP. Fig. 3a illustrates the XRD patterns of Ru/Ru_xFe-CoP, Ru, Fe-CoP and Fe-CoP. The observed peaks at 31.6°, 36.3°, 46.2°, 48.1°, and 56.7° in the Fe-CoP sample correspond to the crystallographic planes (011), (111), (112), (211), and (301) of CoP, respectively. Notably, no additional peaks associated with Fe are detected, and there is no significant shift in the diffraction peaks, which may be due to the fact that the Fe atoms occupy the positions of the Co atoms in the cobalt phosphide and the radii of the Fe and Co atoms are close to each other. The Ru_xFe-CoP displays an orthorhombic crystal system similar to that of Fe-CoP. However, its characteristic XRD diffraction peaks are shifted to the low-angle direction by about 0.3°, indicating a slight expansion distortion in the CoP lattice caused by the incorporation of Ru. For Ru/Ru_xFe-CoP, the characteristic diffraction peaks attributed to CoP show similar low-angle shifts. In addition, three characteristic diffraction peaks at 38.4°, 42.1°, and 44.0° can be attributed to the (100), (002), and (101) crystal planes of the hexagonal phase metal Ru. In summary, the highly coupled Ru/Ru_xFe-CoP heterojunction catalysts have been successfully synthesized.

The as-prepared materials are further investigated by X-ray photoelectron spectroscopy (XPS) to gain insight into the electronic interactions in the Ru/Ru_xFe-CoP Mott Schottky heterostructure. XPS spectra demonstrated the presence of Ru, Co, Fe, and P elements on the Ru/Ru_xFe-CoP and Ru_xFe-CoP surfaces, whereas no signals of Ru elements are detected in Fe-CoP (Fig. 3b). In addition, no signals of elemental Al are observed in the high-resolution Al 2p spectrum of Ru/Ru_xFe-CoP and Ru_xFe-CoP, proving that Al is almost removed during the etching process (Figure S7). The high-resolution XPS spectra of Co 2p and Fe 2p for Ru/Ru_xFe-CoP, Ru_xFe-CoP, and Fe-CoP are shown in Fig. 3c-d. In the case of Fe-CoP, Co 2p peaks can be deconvoluted into two pairs of spin-orbit double peaks, accompanied by satellite peaks. The peaks at 778.6 and 793.6 eV can be attributed to Co-P bonds, while the peaks at 782.1 and 797.7 eV are indicative of Co-O bonds, which may be the result of surface oxidation brought on by air exposure. The peak observed in the Fe 2p spectrum at 707.1 eV can be attributed to the Fe-P bond as well, while the two peaks at 710.9 eV and 714.1 eV correspond to Fe²⁺ and Fe³⁺, respectively. Notably, the Co-P bond in Ru, Fe-CoP shifted to 778.9 eV whereas the Fe-P bond shifted to 707.2 eV in comparison with Fe-CoP. The introduction of Ru may effectively regulate the electron density around the Co and Fe atoms, leading to a positive binding energy shift. After constructing the Mott-Schottky heterointerface, Co 2p and Fe 2p in Ru/Ru_xFe-CoP show a more significant trend of positive shift in binding energy, with the Co-P bond positively shifted by about 0.5 eV and the Fe-P bond positively shifted by about 0.3 eV. This implies that strong electronic interactions occur around the heterointerface, which further induces a redistribution of the charge density at the interface. Co and Fe in higher oxidation states are known to provide enhanced catalytic activity for OER [55]. On the contrary, the binding energy of Ru 3p shows an opposite trend, as shown in Fig. 3e. For metallic Ru, Ru 3p can be deconvoluted into two pairs of double peaks, where Ru 3p_{3/2} and Ru 3p_{1/2} at 461.5 and 483.7 eV are attributed to Ru-P, whereas the peaks at

464.8 and 486.8 eV are likely to originate from the slightly oxidized Ru⁴⁺ species on the surface. In comparison to metallic Ru, Ru_xFe-CoP demonstrates a negative shift in the Ru-P binding energy by approximately 0.5 eV, while it exhibits a significant negative shift in binding energy of about 0.6 eV in Ru/Ru_xFe-CoP, which is opposite to the trend of the binding energy shifts exhibited in Co and Fe, suggesting that the strong interactions between Ru and Co/Fe drive the transfer of electrons from Co/Fe to Ru, resulting in a significant accumulation of electrons at the Ru site. The electron-rich Ru sites, on the other hand, not only optimize the free energy of hydrogen adsorption, but also promote the H₂O dissociation more efficiently [34]. Furthermore, the spectra of P 2p (Fig. 3f) exhibits two distinct peaks located near binding energies of 129.8 and 130.7 eV corresponding to the P 2p_{1/2} and P 2p_{3/2} of the P-M bond, whereas the broad peak at 134.1 eV is attributed to the phosphates. Interestingly, there is a significant positive shift in the binding energy of P 2p in Ru/Ru_xFe-CoP and Ru_xFe-CoP compared to Fe-CoP, suggesting that electrons are transferred from Co or Fe to Ru via bridging P. In conclusion, the binding energy shift confirms the existence of strong electronic interactions between Ru and Co/Fe. The doping of Ru elements and the Mott-Schottky effect contribute to a multilevel charge redistribution in Ru/Ru_xFe-CoP, leading to an accelerated electron transfer from Co and Fe to Ru. The interfacial charge redistribution plays a key role in surface chemisorption properties and catalytic kinetics.

3.2. Electrocatalytic performance and analysis of Ru/Ru_xFe-CoP

In order to gain insight into the electrochemical activity of Ru/Ru_xFe-CoP, the HER catalytic activity is first evaluated using a standard three-electrode setup in N₂ saturated 1 M KOH. In addition, the electrocatalytic activities of Ru_xFe-CoP, Fe-CoP, CoP, Ni foam, and commercial Pt/C were measured as controls. Fig. 4a-b shows the iR-corrected linear sweeping voltammetry (LSV) curves for different catalysts and the corresponding overpotentials at different current densities. The bare Ni foam exhibits low HER activity with an overpotential of 228 mV at a current density of 10 mA cm⁻², suggesting that the bare Ni foam hardly has any HER activity at low potentials. In addition, CoP and Fe-CoP exhibited relatively poor HER activity, with overpotentials of 118 and 76 mV at 10 mA cm⁻², respectively. For Ru_xFe-CoP, the electronic interactions between Ru and Co/Fe play a crucial role in governing the electronic structure of the Ru active sites, which leads to a significant improvement in the HER performance, with an overpotential of only 36 mV at 10 mA cm⁻², close to that of Pt/C (35 mV). The HER performance of Ru/Ru_xFe-CoP is further enhanced after the establishment of Mott-Schottky heterojunction, requiring only 23 mV overpotential to achieve a current density of 10 mA cm⁻². Furthermore, the highly open three-dimensional array structure facilitates the diffusion and penetration of the electrolyte while ensuring the accessibility of the active sites and accelerates the rapid desorption of the gas products. Consequently, it leads to a significant improvement in the electrocatalytic activity at high current densities, with overpotentials of 84, 145, and 207 mV at 100, 500, and 1000 mA cm⁻², respectively, which is superior to that of the majority of reported Ru-based HER catalysts (Fig. 4h and Table S1). In order to gain insight into the HER kinetics of each sample, the corresponding Tafel slopes are determined by linearly fitting the polarization curves. The Tafel slope for Ru/Ru_xFe-CoP, as shown in Fig. 4c, is 37.8 mV dec⁻¹, lower than that of control samples such as Ru_xFe-CoP (47.7 mV dec⁻¹), Fe-CoP (51.1 mV dec⁻¹), and CoP (58.6 mV dec⁻¹), and even lower than that of commercial Pt/C (39.3 mV dec⁻¹), which implies faster HER reaction kinetics. Moreover, the exchange current density (j_0) can be obtained by extrapolating the Tafel curve to zero overpotential for evaluating the intrinsic HER performance of the electrocatalyst. The j_0 of Ru/Ru_xFe-CoP reaches 2.3 mA cm⁻², which is notably higher than that of CoP (0.26 mA cm⁻²), Fe-CoP (0.42 mA cm⁻²), and Ru_xFe-CoP (1.6 mA cm⁻²), suggesting that the incorporation of Ru and the presence of Mott-Schottky heterojunctions

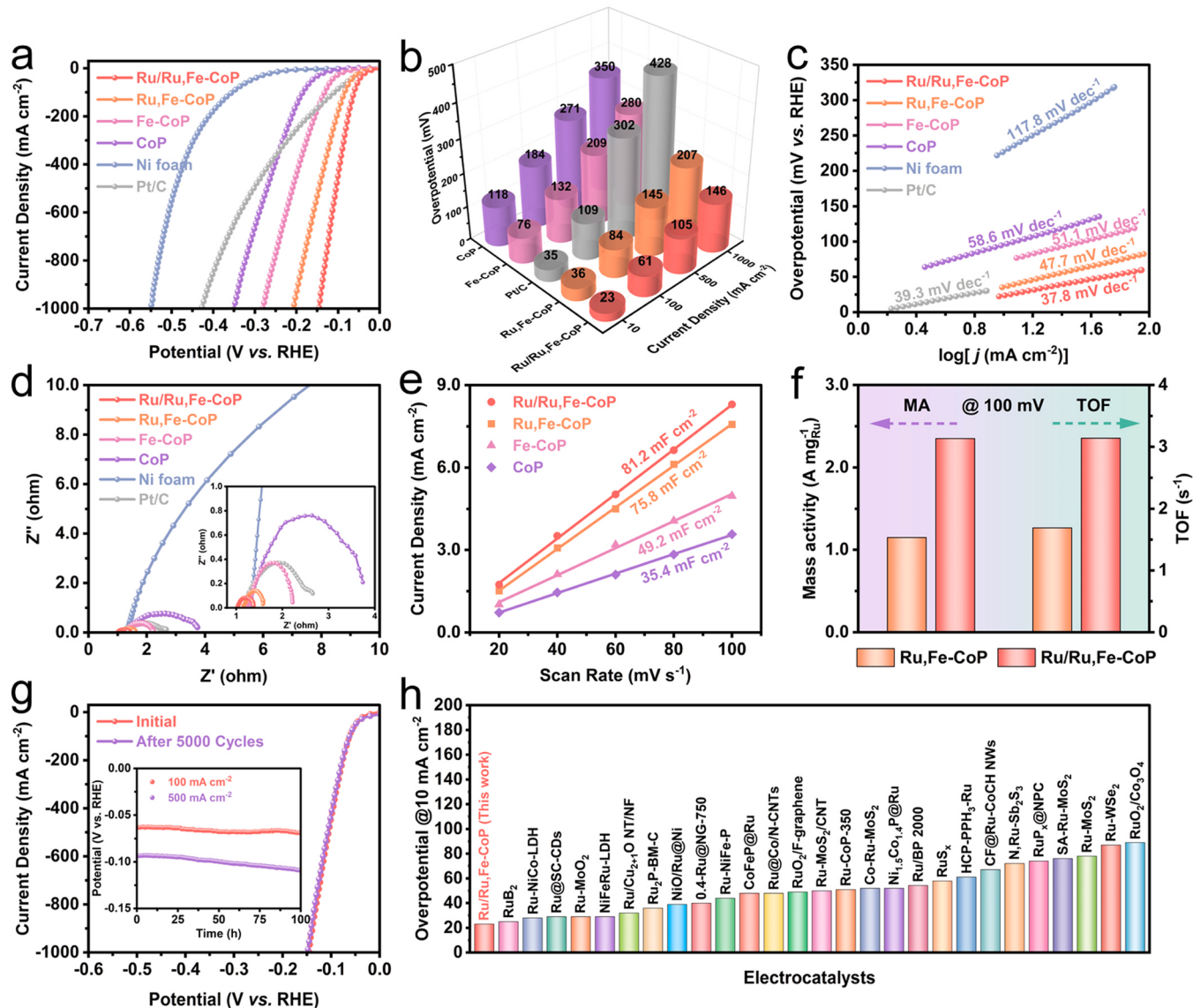


Fig. 4. a) HER polarization curves of Ru/Ru,Fe-CoP, Ru,Fe-CoP, Fe-CoP, CoP, Ni foam and Pt/C. b) Corresponding overpotentials at different current densities. c) Tafel plots. d) Nyquist plots. e) Electrochemically active surface area evaluation. f) Mass activity and turnover of frequency g) Polarization curve initial and after 5000 CV cycles. Inset: chronopotentiometric curves of Ru/Ru,Fe-CoP at the constant currents of 100 and 500 mA cm^{-2} . h) Performance comparison with reported Ru-based HER catalysts.

can significantly facilitate the transport of electrons between the catalyst surface and electrolyte. Furthermore, electrochemical impedance spectroscopy (EIS) revealed that Ru/Ru,Fe-CoP exhibited the lowest charge transfer resistance (R_{ct}), which further demonstrated that the unique structure of Ru/Ru,Fe-CoP greatly improved the charge transfer (Fig. 4d).

To further clarify the origin of the superior HER activity of Ru/Ru,Fe-CoP, the electrochemical active area (ECSA) of each catalyst was evaluated (Figure S8). As shown in Fig. 4e, Ru/Ru,Fe-CoP possessed the largest double-layer capacitance (81.2 mF cm^{-2}), slightly higher than that of Ru,Fe-CoP (75.8 mF cm^{-2}), and approximately two times higher than that of Fe-CoP (49.2 mF cm^{-2}) and CoP (35.4 mF cm^{-2}), which implies that the incorporation of Ru greatly increases the number of active sites, meanwhile the heterogeneous interfaces provide more active sites for the electrocatalytic process. Ru/Ru,Fe-CoP exhibits the highest ECSA-normalised current density over the entire potential range, demonstrating the highest intrinsic HER activity (Figure S9). In order to further confirm the intrinsic activity of Ru species in Ru/Ru,Fe-CoP and Ru,Fe-CoP, Ru mass normalized activity (MA) and turnover of frequency

(TOF) values are calculated, respectively (Figure S10 and S11). As shown in Fig. 4f, Ru/Ru,Fe-CoP exhibits higher mass activity and TOF values than Ru,Fe-CoP at an overpotential of 100 mV, suggesting that the Ru species in Ru/Ru,Fe-CoP has higher intrinsic activity. Furthermore, for revealing the contribution of different Ru species in Ru/Ru,Fe-CoP, KSCN and EDTA are employed as poisoning species (Figure S12 and S13), where EDTA mainly binds to individual Ru sites, while SCN^- tends to adsorb both Ru nanoparticles and Ru sites [30,56]. With the addition of KSCN, Ru/Ru,Fe-CoP and Ru,Fe-CoP exhibit an obvious reduction in current density. And the overpotential of Ru/Ru,Fe-CoP increased much more slowly than that of Ru,Fe-CoP after the addition of EDTA, which shows that the synergistic effect of different Ru species in Ru/Ru,Fe-CoP promotes alkaline HER catalysis, but the Ru nanoparticles are still the mainly active sites. In addition, the long-term stability at high current density is a key parameter to determine whether the catalyst has a practical application prospect, cyclic voltammetry tests and chronopotentiometric tests are carried out for Ru/Ru,Fe-CoP. As shown in Fig. 4g, after 5000 cyclic CV accelerated degradation tests, the polarization curve of Ru/Ru,Fe-CoP is almost unchanged compared to the initial

curve, which proved the excellent durability of the catalyst. The continuous operation at 100 mA cm^{-2} and 500 mA cm^{-2} for 100 h also exhibit excellent HER stability, demonstrating the excellent electrochemical durability and industrial electrocatalytic potential of Ru/Ru, Fe-CoP. The XRD patterns of Ru/Ru,Fe-CoP after HER stability tests showed no change in the physical phase structure, and the characteristic diffraction peaks associated with CoP and Ru could still be observed (Figure S14). SEM and TEM images proved that the original nanowire morphology could be preserved better and the presence of heterogeneous structure could still be observed in HRTEM images (Figure S15). In addition, high-resolution XPS spectra before and after the HER stability tests showed no changes in the valence states of the elements (Figure S16). These characterizations demonstrate the excellent HER stability of the Ru/Ru,Fe-CoP catalyst.

The efficiency of overall water splitting is limited by the complex four-electron transfer process of OER. In view of the multiple active sites in Ru/Ru,Fe-CoP, the OER electrocatalytic properties are examined as well, and the other samples are measured under the same conditions for comparison. Fig. 5a-b shows the OER polarization curves of each catalyst and the corresponding overpotentials required to reach different current densities, respectively. CoP exhibits better OER catalytic activity than bare Ni foam, requiring only 264 mV overpotential to drive a current density of 10 mA cm^{-2} , which is slightly higher than that of commercial RuO₂. The incorporation of Fe or Ru into CoP results in varying degrees of enhancement in its OER catalytic activity, with Fe-CoP and Ru,Fe-CoP achieving overpotentials of 237 and 228 mV, respectively, at a current density of 10 mA cm^{-2} . Ru/Ru,Fe-CoP exhibits the highest current response over the entire OER potential range, providing 10, 100, 500 and 1000 mA cm⁻² current densities at only 206, 241, 292 and 345 mV, respectively, which meet the requirements of commercial water electrolysis. The OER kinetics are further investigated by Tafel plots. As shown in Fig. 5c, the Ru/Ru,Fe-CoP exhibits the lowest

Tafel slope of 37.1 mV dec^{-1} in comparison with that of Ru,Fe-CoP (45.3 mV dec^{-1}), Fe-CoP (55.6 mV dec^{-1}), CoP ($104.2 \text{ mV dec}^{-1}$), RuO₂ (70.3 mV dec^{-1}), and Ni foam ($145.7 \text{ mV dec}^{-1}$), indicating more favorable OER kinetics on the Ru/Ru,Fe-CoP. The ECSA normalized polarization curves reflect that Ru/Ru,Fe-CoP possesses the highest intrinsic activity (Figure S17). Moreover, Ru/Ru,Fe-CoP shows the highest TOF value and MA among all the samples, confirming the advantage of Ru/Ru,Fe-CoP as a better OER catalyst (Figure S18 and S19). Notably, the remarkable OER activity and Tafel slope of Ru/Ru,Fe-CoP are superior to those of recently reported OER electrocatalysts (Fig. 5f and Table S2). Electrochemical impedance spectroscopy (EIS) is conducted to further investigate the reaction kinetics. Fig. 5d clearly reveals the smallest charge transfer resistance (R_{ct}) of Ru/Ru,Fe-CoP, indicating the fastest catalytic reaction kinetics and rapid charge transfer. In addition, CV cycling and chronoamperometry tests are performed to assess the durability of Ru/Ru,Fe-CoP during the OER process. As depicted in Fig. 5e, the LSV curve of Ru/Ru,Fe-CoP slightly decreases before and after 5000 CV cycles, and the chronoamperometry test result (Fig. 5e inset) demonstrate that the catalyst is able to operate stably for 100 h at high current densities of 100 and 500 mA cm⁻², which proves the excellent OER stability of Ru/Ru,Fe-CoP in alkaline electrolytes. Subsequently, XRD, SEM, TEM and XPS are also employed to analyze the structure, morphology and surface state of Ru/Ru,Fe-CoP after the OER stability test (Figure S20-S22). Ru/Ru,Fe-CoP still shows CoP and Ru-related XRD characteristic diffraction peaks after the OER test, which proves the high structural stability of Ru/Ru,Fe-CoP during the OER process, while some other low-intensity peaks can be attributed to the surface oxidation and reconstruction of the catalyst. SEM and TEM images show that Ru/Ru,Fe-CoP is basically able to maintain the morphology of the nanowires. HRTEM image demonstrates that the surface of the catalyst is oxidized to CoOOH, whereas CoP and Ru-related lattice fringes can still be observed in the inner part of the

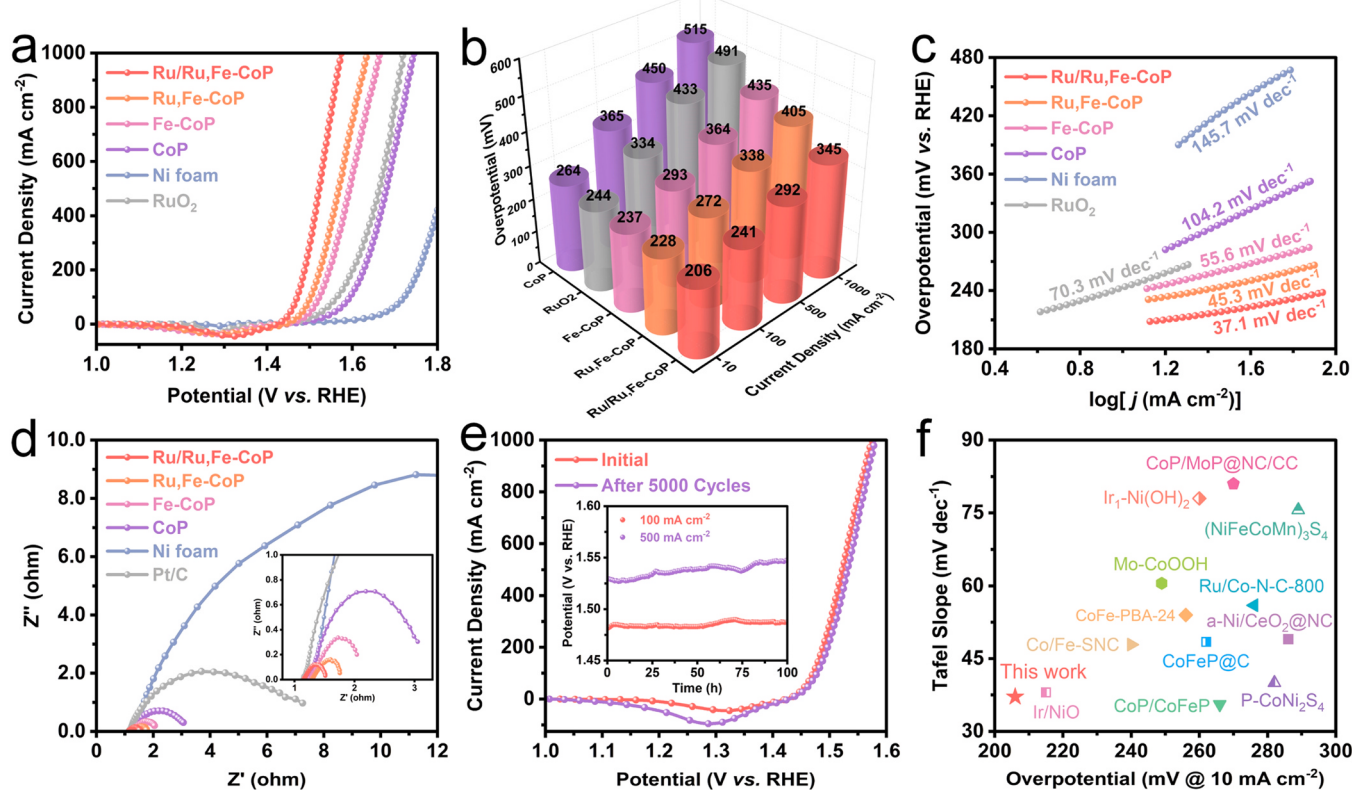


Fig. 5. a) OER polarization curves of Ru/Ru,Fe-CoP, Ru,Fe-CoP, Fe-CoP, CoP, Ni foam and RuO₂. b) Corresponding overpotentials at different current densities. c) Tafel plots. d) Nyquist plots. e) Polarization curve initial and after 5000 CV cycles. Inset: chronopotentiometric curves of Ru/Ru,Fe-CoP at the constant currents of 100 and 500 mA cm⁻². f) Performance comparison with reported OER catalysts.

catalyst, which is further evidence of its excellent structural stability. Only the oxidation states of the relevant elements can be detected in the high-resolution XPS spectra of Co, Fe, Ru and P, confirming the formation of metal hydroxyl oxides on the catalyst surface during the OER process. In summary, the above analysis demonstrates the high structural stability of Ru/Ru,Fe-CoP during the OER process and shows that the reconstruction occurs only at the surface level.

3.3. Energy band structure analysis of Ru/Ru,Fe-CoP

In order to better understand the Mott-Schottky contact between Ru and Ru,Fe-CoP in Ru/Ru,Fe-CoP catalysts toward enhanced HER and OER catalytic activity, the bandgap and work function have been investigated firstly by ultraviolet and visible spectroscopy (UV-Vis) and ultraviolet photoelectron spectroscopy (UPS) (Figure S23). The Tauc plots derived from the UV-visible spectra give band gaps of 2.62 eV, 2.48 eV, and 2.31 eV for CoP, Fe-CoP, and Ru,Fe-CoP, respectively, which implies that the co-doping of Ru and Fe improves the electrical conductivity of CoP. The cut-off energy ($E_{\text{cut-off}}$) values for CoP, Fe-CoP and Ru,Fe-CoP are given by the normalized secondary electron cut-off (SECO) spectra, and the corresponding work functions (Φ) are calculated to be 4.13 eV, 3.95 eV and 3.72 eV, respectively [45]. Combined with the valence band spectra, the energy level structures of CoP, Fe-CoP and Ru,Fe-CoP are determined (Fig. 6a), where the Fermi energy levels gradually move from the centre of the forbidden bands towards the bottom of the conductive bands with the incorporation of Ru and Fe [57, 58]. The Φ for the metal Ru, as determined from DFT calculations (Figure S29), is 4.75 eV (0.25 V vs RHE). According to semiconductor physics, when the Fermi energy level of the semiconductor material is lower than that of the metal material, electrons will be transferred from the semiconductor to the metal across the Schottky interface [39]. Ru, Fe-CoP and metal Ru have the largest energy level difference; in this case, it will be more favourable for electrons to migrate from the Ru, Fe-CoP side to the metal Ru region. The energy band diagrams of

before and after Ru and Ru,Fe-CoP contact are shown in Fig. 6b. The built-in electric field induced by the Mott-Schottky heterojunction will drive electrons across the interface from Ru,Fe-CoP to Ru, which is consistent with the results obtained by XPS. In order to quantitatively analyse the electron transfer phenomenon, we calculated the charge density differences of Ru/Ru,Fe-CoP (Fig. 6c), where the red and green regions refer to the electron accumulation and electron depletion regions, respectively. Apparently the coupling between Ru and Ru,Fe-CoP induces a redistribution of the local charge at the interface, leading to the migration of electrons from Ru,Fe-CoP to Ru, which is consistent with the analyses of XPS and UPS. The calculated Φ of Ru,Fe-CoP is 4.07 eV, which is 0.68 eV lower than that of Ru (Figure S30), satisfying the prerequisites for the formation of Schottky barriers and the theoretical feasibility of interfacial charge transfer from Ru,Fe-CoP to Ru. The significant accumulation of electrons on the Ru side greatly enhances the electron-donating ability of Ru to the electrolyte molecules, in addition to the fact that the electron-rich Ru component also plays a crucial role in the water dissociation process [47]. On the other hand, the redistribution of electrons at the heterogeneous interface results in obvious energy band bending, pulling down the valence band of Ru, Fe-CoP, which means that a more positive charged centre would be formed on the surface of Ru,Fe-CoP, facilitating the transfer of electrons from the OH⁻ to the valence band of Ru,Fe-CoP, and improving the OER activity.

The Gibbs free energy of hydrogen adsorption (ΔG_{H^*}) proves to be the most important descriptor for HER activity evaluation. In general, a moderate ΔG_{H^*} value is preferred to ensure fast hydrogen adsorption and desorption. The optimized models for H* adsorption on Ru, Ru,Fe-CoP and Ru/Ru,Fe-CoP surfaces are depicted in Figure S24. As shown in Fig. 6d, the ΔG_{H^*} of Ru/Ru,Fe-CoP (-0.248 eV) is closer to the ideal value of 0 eV compared to Ru (-0.424 eV) and Ru,Fe-CoP (0.302 eV), which implies thermo-neutral adsorption/desorption of the H atoms on Ru/Ru,Fe-CoP in the HER process and inherent high catalytic activity. The kinetics of the OER process is determined by the efficiency of

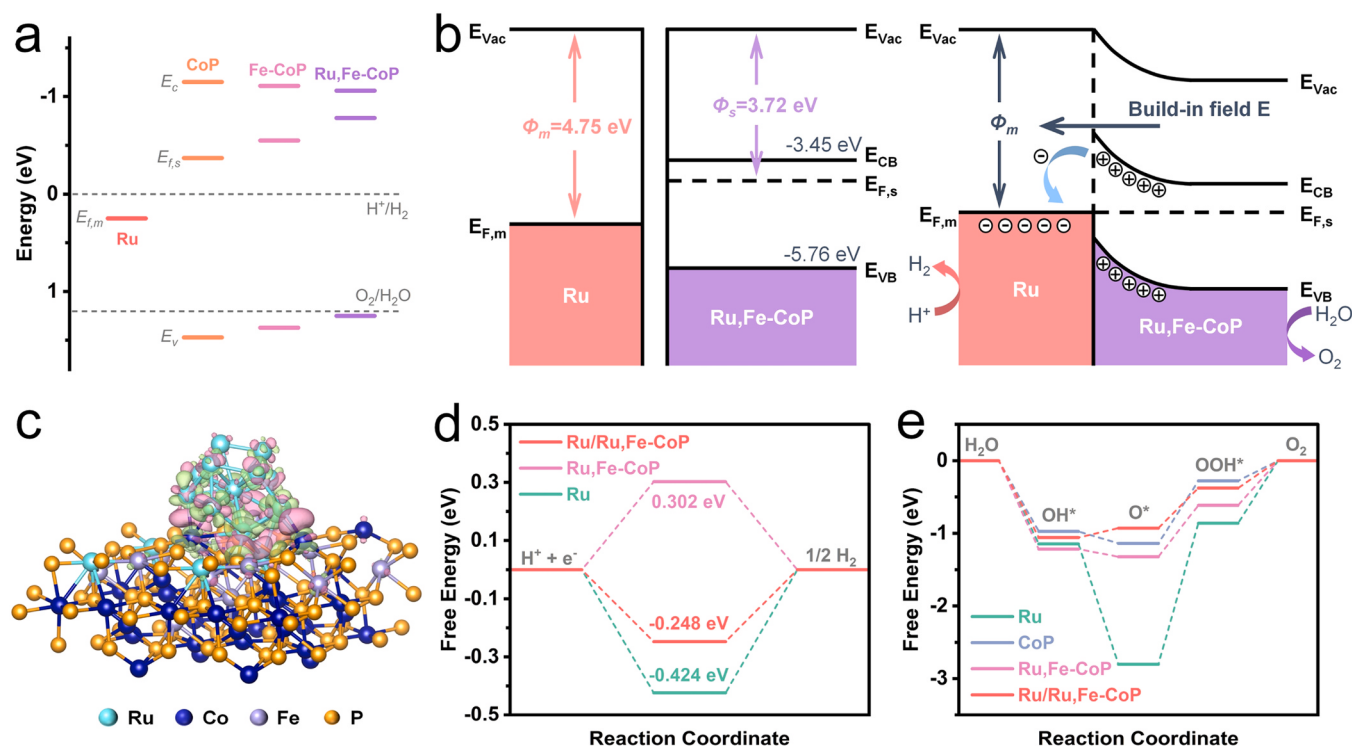


Fig. 6. a) Energy band diagram of Ru,Fe-CoP, Fe-CoP and CoP, b) Energy band diagram of Ru and Ru,Fe-CoP before and after Schottky contact, c) Charge density difference plot at the Ru/Ru,Fe-CoP interface, d) The calculated H* adsorption Gibbs free energy, e) Comparison of free energy of different elementary steps in OER on Ru, CoP, Ru,Fe-CoP and Ru/Ru,Fe-CoP.

electron transfer from the oxygen intermediate to the active site, which is driven by the electron-deficient sites. Based on the structural models (Figure S25–S28) of Ru, CoP, Ru_xFe-CoP, and Ru/Ru_xFe-CoP, the free energy diagrams of four OER steps with the applied equilibrium potential ($U = 1.23$ V) are calculated in Fig. 6e. Apparently, the rate-determining step (RDS) of the four optimized structures is the formation of activated OOH* intermediates. Ru has the highest RDS energy barrier of 1.94 eV. Furthermore, the RDS energy barrier of Ru/Ru_xFe-CoP reduces to 0.55 eV in comparison to CoP (0.86 eV) and Ru_xFe-CoP (0.71 eV), indicating that Ru/Ru_xFe-CoP is thermodynamically more favourable for catalytic OER. The above results clearly demonstrate that the charge modulation of the Mott-Schottky effect in Ru/Ru_xFe-CoP effectively induced electron redistribution, leading to the reduction of the adsorption energy of H* intermediates in the HER process and the energy barrier for the formation of *OOH in the OER decisive step.

3.4. Overall water/seawater splitting performance

Finally, the alkaline electrolytic cell was assembled with Ru/Ru_xFe-CoP as both anode and cathode to assess the overall water splitting performance, and the electrolytic cell consisting of RuO₂ as anode and Pt/C as cathode was also fabricated for comparison (Figure S31). Fig. 7a exhibits LSV curves of Ru/Ru_xFe-CoP_(+, -) and Pt/C||RuO₂₍₊₎ for overall water splitting, revealing that Ru/Ru_xFe-CoP_(+, -) has higher activity than that of Pt/C||RuO₂. Furthermore, Ru/Ru_xFe-CoP_(+, -) possesses remarkable overall water splitting activity at extremely low cell voltages of 1.451, 1.531, and 1.654 V at 10, 100, and 500 mA cm⁻², respectively (Fig. 7b). In consideration of the exceptional HER and OER performance of Ru/Ru_xFe-CoP in 1 M KOH electrolytes, we further evaluated its HER and OER performance in both simulated seawater (1 M KOH + 0.5 M NaCl) and alkaline seawater (1 M KOH + seawater) electrolytes (Figure S32). The performance of Ru/Ru_xFe-CoP in 1 M KOH seawater is

comparatively inferior to that in simulated seawater and 1 M KOH for both HER and OER. The diminished catalytic performance of electrocatalysts in seawater mostly arises from the blockage of active sites and the contamination of the surface by ions or particles present in the seawater, as extensively documented in previous research. Figure S32b and S32e summarizes the overpotentials required for Ru/Ru_xFe-CoP as HER and OER electrocatalysts to drive current densities of 10, 100 and 500 mA cm⁻² in different electrolytes. It is noteworthy that even at the higher current density of 1000 mA cm⁻², the overpotential required for OER is only 320 mV, which is much lower than the overpotential of 480 mV required to initiate the chloride evolution reaction. The long-term stability of Ru/Ru_xFe-CoP electrode for HER and OER was tested at 100 and 500 mA cm⁻² in 1 M KOH + seawater electrolyte for 100 h (Figure S32c and S32f). The Ru/Ru_xFe-CoP displays essentially constant operating potentials for 100 h, exhibiting satisfactory stability. SEM after the stability test showed that the nanowire morphology of Ru/Ru_xFe-CoP are well preserved (Figure S33–S34). Following the stability tests, the tested seawater electrolyte was examined for hypochlorite formation using N,N-diethyl-p-phenylenediamine (DPD) reagent. As shown in Figure S35, there was no colour change in the reagent, indicating that no hypochlorite was formed during the OER process. The iR-corrected LSV curves of two-electrode Ru/Ru_xFe-CoP assembled electrolyzer exhibit the outstanding overall seawater splitting performance (Fig. 7c). Specifically, in the alkaline natural seawater, the electrolyzer shows a slight performance decay but still achieves current densities of 100 and 500 mA cm⁻² at low cell voltages of only 1.58 and 1.75 V. Moreover, the Faradaic efficiency (FE) of the overall seawater electrolysis was measured by the drainage approach. The obtained data is shown in Fig. 7d and indicates that the quantities of O₂ and H₂ gas generated roughly match the theoretical values, demonstrating approximately 100% Faraday efficiency. In addition, the Ru/Ru_xFe-CoP_(+, -) electrolyzers exhibited excellent stability for 100 h at current

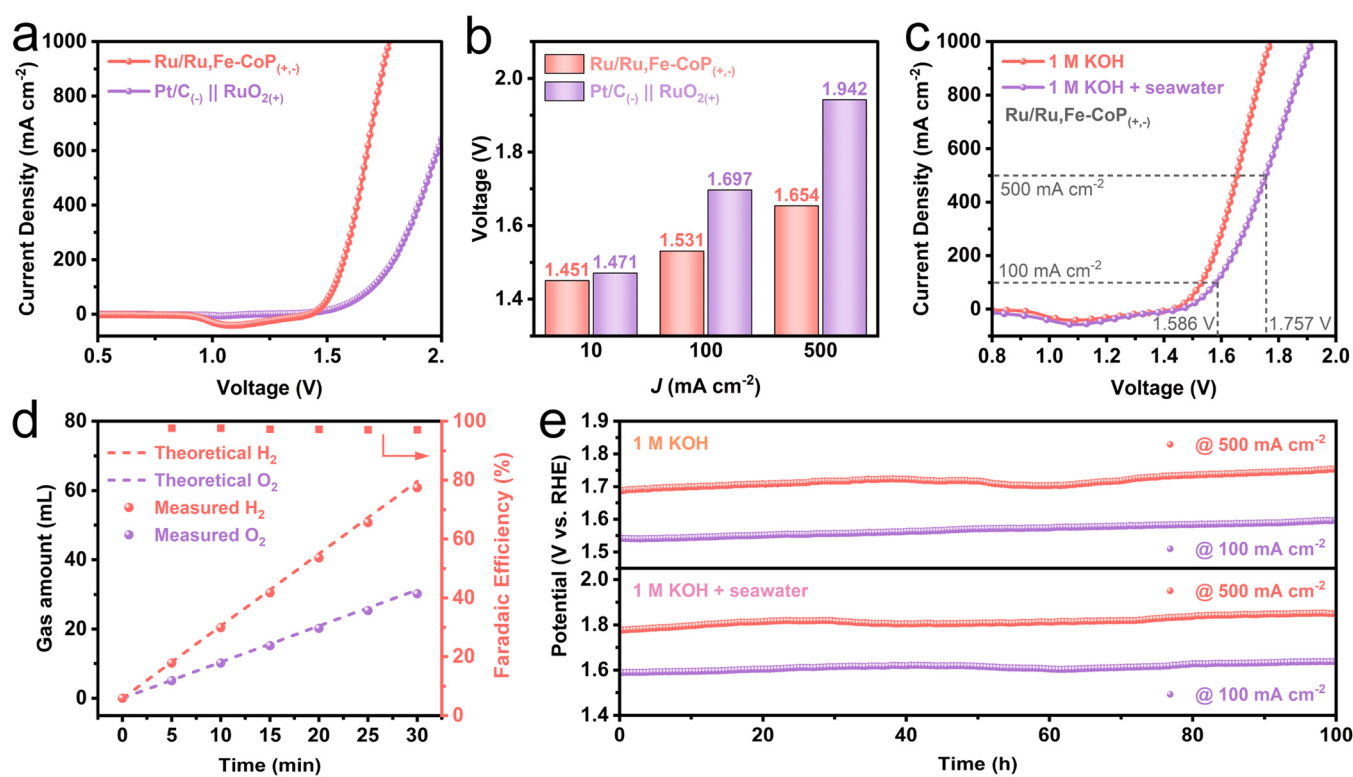


Fig. 7. a) Polarization curves of Ru/Ru_xFe-CoP_(+, -) and Pt/C||RuO₂ electrolyzers in 1 M KOH electrolyte. b) Corresponding cell potentials at different current densities. c) Overall water/seawater electrolysis performance of Ru/Ru_xFe-CoP_(+, -) in 1 M KOH and 1 M KOH seawater electrolytes. d) Measured and theoretical gaseous products from the Ru/Ru_xFe-CoP_(+, -) at a current density of 150 mA cm⁻² in 1 M KOH seawater electrolyte. e) Chronopotentiometric curves of Ru/Ru_xFe-CoP_(+, -) at a constant current density of 100 and 500 mA cm⁻² for overall water/seawater splitting in 1 M KOH and 1 M KOH seawater.

densities of 100 and 500 mA cm⁻² in both 1 M KOH and 1 M KOH + seawater electrolytes (Fig. 7e), showing a promising application as a bifunctional electrocatalyst for seawater electrolysis.

4. Conclusions

In summary, the Ru/Ru_xFe-CoP Mott-Schottky nanowire array was successfully fabricated as a bifunctional electrocatalyst for water/seawater splitting. Experimental results demonstrate that cooperative doping of Ru and Fe in cobalt phosphide effectively reduces the work function of the host CoP. Combined with theoretical calculations, it is demonstrated the strong interfacial built-in electric field induced by the enlarged work function difference leads to asymmetric charge distributions at the Ru/Ru_xFe-CoP interfaces, with the negative charge-enriched Ru side and positive charge-enriched Ru_xFe-CoP area being responsible for optimizing the adsorption strength of HER and OER intermediates, respectively. The as-obtained Ru/Ru_xFe-CoP catalyst shows remarkable performance with ultra-high current density of 1000 mA cm⁻² for HER and OER at 1 M KOH achieved with only 146 mV and 345 mV, respectively, and also exhibits excellent electrocatalytic performance and stability in real seawater media. Notably, the Ru/Ru_xFe-CoP_(+, -) electrolyzer in 1.0 M KOH produces 500 mA cm⁻² at a low voltage of 1.654 V, significantly exceeding that of Pt/C||RuO₂ and many reported noble metal-based catalysts. Furthermore, the Ru/Ru_xFe-CoP-based alkaline seawater electrolyzer show low potential requirement, high stability, and high Faradaic efficiency of 97.1%. The rational construction of Mott-Schottky heterogeneous components to modulate the surface charge distribution to obtain excellent electrocatalytic activity will provide a novel strategy for us to explore other superior bifunctional electrocatalysts.

CRediT authorship contribution statement

Zhuoping Wang: Writing – review & editing, Writing – original draft, Investigation, Data curation, Conceptualization. **Shuai Wang:** Writing – review & editing, Funding acquisition, Formal analysis.

Declaration of Competing Interest

The authors declare that they have no known competing financial interests or personal relationships that could have appeared to influence the work reported in this paper.

Data availability

Data will be made available on request.

Acknowledgements

The authors thank Shiyanjia Lab (www.shiyanjia.com) for the XPS and UPS analysis. The authors thank the Analytical and Testing Center of Huazhong University of Science and Technology, the Wuhan National Laboratory for Optoelectronics. This work was financially supported by the Key Research and Development Program of Hubei Province (No.2022BAA026), the Nation Key R&D Program China (Grant Numbers: 2018YFA0703200) and the National Natural Science Foundation of China (Grant Numbers: 61890941 and 51772110).

Appendix A. Supporting information

Supplementary data associated with this article can be found in the online version at [doi:10.1016/j.apcatb.2024.124002](https://doi.org/10.1016/j.apcatb.2024.124002).

References

- [1] Z.W. Seh, J. Kibsgaard, C.F. Dickens, I. Chorkendorff, J.K. Nørskov, T.F. Jaramillo, Combining theory and experiment in electrocatalysis: insights into materials design, *Science* 355 (2017) ead4998.
- [2] I. Staffell, D. Scaman, A. Velazquez Abad, P. Balcombe, P.E. Dodds, P. Ekins, N. Shah, K.R. Ward, The role of hydrogen and fuel cells in the global energy system, *Energy Environ. Sci.* 12 (2019) 463–491.
- [3] Y. Liu, Q. Wang, J. Zhang, J. Ding, Y. Cheng, T. Wang, J. Li, F. Hu, H.B. Yang, B. Liu, Recent advances in carbon-supported noble-metal electrocatalysts for hydrogen evolution reaction: syntheses, structures, and properties, *Adv. Energy Mater.* 12 (2022) 2200928.
- [4] F. Razmjooei, T. Morawietz, E. Taghizadeh, E. Hadjixenophontos, L. Mues, G. Gerle, B.D. Wood, C. Harms, A.S. Gago, S.A. Ansar, K.A. Friedrich, Increasing the performance of an anion-exchange membrane electrolyzer operating in pure water with a nickel-based microporous layer, *Joule* 5 (2021) 1776–1799.
- [5] X. Liu, J. Chi, H. Mao, L. Wang, Principles of designing electrocatalyst to boost reactivity for seawater splitting, *Adv. Energy Mater.* 13 (2023) 2301438.
- [6] H. Zhao, Z.-Y. Yuan, Progress and perspectives for solar-driven water electrolysis to produce green hydrogen, *Adv. Energy Mater.* 13 (2023) 2300254.
- [7] M.L. Frisch, T.N. Thanh, A. Arinchtein, L. Hager, J. Schmidt, S. Brückner, J. Kerres, P. Strasser, Seawater electrolysis using all-PGM-free catalysts and cell components in an asymmetric feed, *ACS Energy Lett.* 8 (2023) 2387–2394.
- [8] C.J. Vörösmarty, P.B. McIntyre, M.O. Gessner, D. Dudgeon, A. Prusevich, P. Green, S. Glidden, S.E. Bunn, C.A. Sullivan, C.R. Liermann, P.M. Davies, Global threats to human water security and river biodiversity, *Nature* 467 (2010) 555–561.
- [9] Y. Gu, N. Nie, J. Liu, Y. Yang, L. Zhao, Z. Lv, Q. Zhang, J. Lai, Enriching H₂O through boron nitride as a support to promote hydrogen evolution from non-filtered seawater, *EcoEnergy* 1 (2023) 405–413.
- [10] W. He, X. Li, C. Tang, S. Zhou, X. Lu, W. Li, X. Li, X. Zeng, P. Dong, Y. Zhang, Q. Zhang, Materials design and system innovation for direct and indirect seawater electrolysis, *ACS Nano* 17 (2023) 22227–22239.
- [11] S. Dresp, F. Dionigi, M. Klingenhof, P. Strasser, Direct electrolytic splitting of seawater: opportunities and challenges, *ACS Energy Lett.* 4 (2019) 933–942.
- [12] F. Dionigi, T. Reier, Z. Pawolek, M. Gleich, P. Strasser, Design Criteria, operating conditions, and nickel–iron hydroxide catalyst materials for selective seawater electrolysis, *ChemSusChem* 9 (2016) 962–972.
- [13] T. Sun, S. Mitchell, J. Li, P. Lyu, X. Wu, J. Pérez-Ramírez, J. Lu, Design of local atomic environments in single-atom electrocatalysts for renewable energy conversions, *Adv. Mater.* 33 (2021) 2003075.
- [14] Z. Li, Z. Wang, S. Xi, X. Zhao, T. Sun, J. Li, W. Yu, H. Xu, T.S. Herring, X. Hai, P. Lyu, M. Zhao, S.J. Pennycook, J. Ding, H. Xiao, J. Lu, Tuning the spin density of cobalt single-atom catalysts for efficient oxygen evolution, *ACS Nano* 15 (2021) 7105–7113.
- [15] T. Sun, Z. Tang, W. Zang, Z. Li, J. Li, Z. Li, L. Cao, J.S. Dominic Rodriguez, C.O. M. Mariano, H. Xu, P. Lyu, X. Hai, H. Lin, X. Sheng, J. Shi, Y. Zheng, Y.-R. Lu, Q. He, J. Chen, K.S. Novoselov, C.-H. Chuang, S. Xi, X. Luo, J. Lu, Ferromagnetic single-atom spin catalyst for boosting water splitting, *Nat. Nanotechnol.* 18 (2023) 763–771.
- [16] X. Li, Y. Fang, J. Wang, H. Fang, S. Xi, X. Zhao, D. Xu, H. Xu, W. Yu, X. Hai, C. Chen, C. Yao, H.B. Tao, A.G.R. Howe, S.J. Pennycook, B. Liu, J. Lu, C. Su, Ordered clustering of single atomic Te vacancies in atomically thin PtTe₂ promotes hydrogen evolution catalysis, *Nat. Commun.* 12 (2021) 2351.
- [17] D. Strmcnik, P.P. Lopes, B. Genorio, V.R. Stamenkovic, N.M. Markovic, Design principles for hydrogen evolution reaction catalyst materials, *Nano Energy* 29 (2016) 29–36.
- [18] Y. Li, Z. Dong, L. Jiao, Multifunctional transition metal-based phosphides in energy-related electrocatalysis, *Adv. Energy Mater.* 10 (2020) 1902104.
- [19] H. Zhang, A.W. Maijenburg, X. Li, S.L. Schweizer, R.B. Wehrsophn, Bifunctional heterostructured transition metal phosphides for efficient electrochemical water splitting, *Adv. Funct. Mater.* 30 (2020) 2003261.
- [20] X. Yu, Y. Lu, J. Shi, X. Hao, Z. Ma, K. Yang, T. Zhang, C. Li, D. Zhang, X. Huang, Y. He, Corrosion-resistant cobalt phosphide electrocatalysts for salinity tolerance hydrogen evolution, *Nat. Commun.* 14 (2023) 7708.
- [21] Z. Pu, T. Liu, I.S. Amiinu, R. Cheng, P. Wang, C. Zhang, P. Ji, W. Hu, J. Liu, S. Mu, Transition-metal phosphides: activity origin, energy-related electrocatalysis applications, and synthetic strategies, *Adv. Funct. Mater.* 30 (2020) 2004009.
- [22] W. Yu, Y. Gao, Z. Chen, Y. Zhao, Z. Wu, L. Wang, Strategies on improving the electrocatalytic hydrogen evolution performances of metal phosphides, *Chin. J. Catal.* 42 (2021) 1876–1902.
- [23] H. Ma, W. Yan, Y. Yu, L. Deng, Z. Hong, L. Song, L. Li, Phosphorus vacancies improve the hydrogen evolution of MoP electrocatalysts, *Nanoscale* 15 (2023) 1357–1364.
- [24] N. Yang, S. Tian, Y. Feng, Z. Hu, H. Liu, X. Tian, L. Xu, C. Hu, J. Yang, Introducing high-valence Iridium single atoms into bimetal phosphides toward high-efficiency oxygen evolution and overall water splitting, *Small* 19 (2023) 2207253.
- [25] L. Huang, R. Yao, X. Wang, S. Sun, X. Zhu, X. Liu, M.G. Kim, J. Lian, F. Liu, Y. Li, H. Zong, S. Han, X. Ding, In situ phosphating of Zn-doped bimetallic skeletons as a versatile electrocatalyst for water splitting, *Energy Environ. Sci.* 15 (2022) 2425–2434.
- [26] X. Zhang, X. Zhang, H. Xu, Z. Wu, H. Wang, Y. Liang, Iron-doped cobalt monophosphide nanosheet/carbon nanotube hybrids as active and stable electrocatalysts for water splitting, *Adv. Funct. Mater.* 27 (2017) 1606635.
- [27] Y. Li, H. Zhang, M. Jiang, Q. Zhang, P. He, X. Sun, 3D self-supported Fe-doped Ni₂P nanosheet arrays as bifunctional catalysts for overall water splitting, *Adv. Funct. Mater.* 27 (2017) 1702513.

- [28] S. Anantharaj, S. Kundu, S. Noda, The Fe Effect": a review unveiling the critical roles of Fe in enhancing OER activity of Ni and Co based catalysts, *Nano Energy* 80 (2021) 105514.
- [29] C. Hu, E. Song, M. Wang, W. Chen, F. Huang, Z. Feng, J. Liu, J. Wang, Partial-single-atom, partial-nanoparticle composites enhance water dissociation for hydrogen evolution, *Adv. Sci.* 8 (2021) 2001881.
- [30] C. Yang, Z. Wu, Z. Zhao, Y. Gao, T. Ma, C. He, C. Wu, X. Liu, X. Luo, S. Li, C. Cheng, C. Zhao, Electronic structure-dependent water-dissociation pathways of ruthenium-based catalysts in alkaline H₂-evolution, *Small* 19 (2023) 2206949.
- [31] L. Hou, H. Jang, X. Gu, X. Cui, J. Tang, J. Cho, X. Liu, Design strategies of ruthenium-based materials toward alkaline hydrogen evolution reaction, *EcoEnergy* 1 (2023) 16–44.
- [32] W.D. Li, Y.X. Zhao, Y. Liu, M.Z. Sun, G.I.N. Waterhouse, B.L. Huang, K. Zhang, T. R. Zhang, S.Y. Lu, Exploiting Ru-induced lattice strain in CoRu nanoalloys for robust bifunctional hydrogen production, *Angew. Chem. Int Ed.* 60 (2021) 3290–3298.
- [33] X. Wu, Z. Wang, D. Zhang, Y. Qin, M. Wang, Y. Han, T. Zhan, B. Yang, S. Li, J. Lai, L. Wang, Solvent-free microwave synthesis of ultra-small Ru-Mo₂C@CNT with strong metal-support interaction for industrial hydrogen evolution, *Nat. Commun.* 12 (2021) 4018.
- [34] J. Mao, C.-T. He, J. Pei, W. Chen, D. He, Y. He, Z. Zhuang, C. Chen, Q. Peng, D. Wang, Y. Li, Accelerating water dissociation kinetics by isolating cobalt atoms into ruthenium lattice, *Nat. Commun.* 9 (2018) 4958.
- [35] C. Cai, K. Liu, Y. Zhu, P. Li, Q. Wang, B. Liu, S. Chen, H. Li, L. Zhu, H. Li, J. Fu, Y. Chen, E. Pensa, J. Hu, Y.-R. Lu, T.-S. Chan, E. Cortés, M. Liu, Optimizing hydrogen binding on ru sites with ruco alloy nanosheets for efficient alkaline hydrogen evolution, *Angew. Chem. Int. Ed.* 61 (2022) e202113664.
- [36] K. Zhang, J. Jia, E. Yang, S. Qi, H. Tian, J. Chen, J. Li, Y. Lou, Y. Guo, Work-function-induced electron rearrangement of in-plane FeP@CoP heterojunction enhances all pH range and alkaline seawater hydrogen evolution reaction, *Nano Energy* 114 (2023) 108601.
- [37] L. Wu, L. Yu, B. McElhenny, X. Xing, D. Luo, F. Zhang, J. Bao, S. Chen, Z. Ren, Rational design of core-shell-structured CoP_x@FeOOH for efficient seawater electrolysis, *Appl. Catal. B Environ.* 294 (2021) 120256.
- [38] L. Wu, L. Yu, F. Zhang, B. McElhenny, D. Luo, A. Karim, S. Chen, Z. Ren, Heterogeneous bimetallic phosphide Ni₂P-Fe₂P as an efficient bifunctional catalyst for water/seawater splitting, *Adv. Funct. Mater.* 31 (2021) 2006484.
- [39] C. Pi, X. Li, X. Zhang, H. Song, Y. Zheng, B. Gao, A. Kizilaslan, P.K. Chu, K. Huo, In-Plane Mott-Schottky effects enabling efficient hydrogen evolution from Mo₅N₆-Mo₂S heterojunction nanosheets in universal-pH electrolytes, *Small* 18 (2022) 2201137.
- [40] X. Wang, X. Zong, B. Liu, G. Long, A. Wang, Z. Xu, R. Song, W. Ma, H. Wang, C. Li, Boosting electrochemical water oxidation on NiFe (oxy) hydroxides by constructing Schottky junction toward water electrolysis under industrial conditions, *Small* 18 (2022) 2105544.
- [41] Q. Wen, K. Yang, D. Huang, G. Cheng, X. Ai, Y. Liu, J. Fang, H. Li, L. Yu, T. Zhai, Schottky heterojunction nanosheet array achieving high-current-density oxygen evolution for industrial water splitting electrolyzers, *Adv. Energy Mater.* 11 (2021) 2102353.
- [42] C. Li, Y. Liu, Z. Zhuo, H. Ju, D. Li, Y. Guo, X. Wu, H. Li, T. Zhai, Local charge distribution engineered by schottky heterojunctions toward urea electrolysis, *Adv. Energy Mater.* 8 (2018) 1801775.
- [43] C. Wang, H. Lu, Z. Mao, C. Yan, G. Shen, X. Wang, Bimetal Schottky heterojunction boosting energy-saving hydrogen production from alkaline water via urea electrocatalysis, *Adv. Funct. Mater.* 30 (2020) 2000556.
- [44] K. He, T. TadesseTsiga, X. Liu, J. Zai, X.-H. Li, X. Liu, W. Li, N. Ali, X. Qian, Utilizing the space-charge region of the FeNi-LDH/CoP p-n junction to promote performance in oxygen evolution electrocatalysis, *Angew. Chem. Int. Ed.* 58 (2019) 11903–11909.
- [45] D. Liang, C. Lian, Q. Xu, M. Liu, H. Liu, H. Jiang, C. Li, Interfacial charge polarization in Co₂P₂O₇@N, P co-doped carbon nanocages as Mott-Schottky electrocatalysts for accelerating oxygen evolution reaction, *Appl. Catal. B Environ.* 268 (2020) 118417.
- [46] X. Xu, A. Cao, W. You, Z. Tao, L. Kang, J. Liu, Assembly of cobalt layered double hydroxide on cuprous phosphide nanowire with strong built-in potential for accelerated overall water splitting, *Small* 17 (2021) 2101725.
- [47] Z.-H. Xue, H. Su, Q.-Y. Yu, B. Zhang, H.-H. Wang, X.-H. Li, J.-S. Chen, Janus Co/CoP nanoparticles as efficient Mott-Schottky electrocatalysts for overall water splitting in wide pH range, *Adv. Energy Mater.* 7 (2017) 1602355.
- [48] S. Zhang, C. Tan, R. Yan, X. Zou, F.-L. Hu, Y. Mi, C. Yan, S. Zhao, Constructing built-in electric field in heterogeneous nanowire arrays for efficient overall water electrolysis, *Angew. Chem. Int. Ed.* 62 (2023) e202302795.
- [49] H.-Y. Chen, L. Yang, R.-X. Wang, W.-J. Zhang, R. Liu, Y.-Z. Yun, N. Wang, S. Ramakrishna, L. Jiao, Y.-Z. Long, Constructing CoO/Mo₂C heterostructures with interfacial electron redistribution induced by work functions for boosting overall water splitting, *Small* 19 (2023) 2304086.
- [50] G. Kresse, J. Furthmüller, Efficiency of ab-initio total energy calculations for metals and semiconductors using a plane-wave basis set, *Comput. Mater. Sci.* 6 (1996) 15–50.
- [51] G. Kresse, J. Furthmüller, Efficient iterative schemes for ab initio total-energy calculations using a plane-wave basis set, *Phys. Rev. B* 54 (1996) 11169–11186.
- [52] J.P. Perdew, K. Burke, M. Ernzerhof, Generalized gradient approximation made simple, *Phys. Rev. Lett.* 77 (1996) 3865–3868.
- [53] G. Kresse, D. Joubert, From ultrasoft pseudopotentials to the projector augmented-wave method, *Phys. Rev. B* 59 (1999) 1758–1775.
- [54] H.J. Monkhorst, J.D. Pack, Special points for Brillouin-zone integrations, *Phys. Rev. B* 13 (1976) 5188–5192.
- [55] H. Wang, T. Zhai, Y. Wu, T. Zhou, B. Zhou, C. Shang, Z. Guo, High-valence oxides for high performance oxygen evolution electrocatalysis, *Adv. Sci.* 10 (2023) 2301706.
- [56] D. Cao, J. Wang, H. Xu, D. Cheng, Construction of dual-site atomically dispersed electrocatalysts with Ru-C5 single atoms and Ru-O₄ nanoclusters for accelerated alkali hydrogen evolution, *Small* 17 (2021) 2101163.
- [57] Y. Song, M. Sun, S. Zhang, X. Zhang, P. Yi, J. Liu, B. Huang, M. Huang, L. Zhang, Alleviating the work function of vein-like Co₃P by Cr doping for enhanced seawater electrolysis, *Adv. Funct. Mater.* 33 (2023) 2214081.
- [58] S. Zhang, C. Zhang, X. Zheng, G. Su, H. Wang, M. Huang, Integrating electrophilic and nucleophilic dual sites on heterogeneous bimetallic phosphide via enhancing interfacial electronic field to boost hydrazine oxidation and hydrogen evolution, *Appl. Catal. B Environ.* 324 (2023) 122207.